

PAPER • OPEN ACCESS

# Non-contact intelligent sensor for recognizing transparent and naked-eye indistinguishable materials based on ferroelectric BiFeO<sub>3</sub> thin films


To cite this article: Shengjie Yin *et al* 2024 *Int. J. Extrem. Manuf.* **6** 055502

View the [article online](#) for updates and enhancements.

You may also like

- [Forming Gas Annealing Induced Degradation in Nanoscale Electrical Homogeneity of Bismuth Ferrite Thin Films](#)  
Yuan-Chang Liang
- [Straintronics: a new trend in micro- and nanoelectronics and materials science](#)  
A A Bukharaev, A K Zvezdin, A P Pyatakov et al.
- [Microstructural, optical, and magnetic properties and specific absorption rate of bismuth ferrite/SiO<sub>2</sub> nanoparticles](#)  
Erna Juwita, Fitria Ayu Sulistiani, Mahardika Yoga Darmawan et al.

# Non-contact intelligent sensor for recognizing transparent and naked-eye indistinguishable materials based on ferroelectric BiFeO<sub>3</sub> thin films

Shengjie Yin<sup>1,2</sup>, Hongyu Li<sup>2,3</sup>, Weiqi Qian<sup>2,3</sup>, Md Al Mahadi Hasan<sup>2,3</sup> and Ya Yang<sup>1,2,3,\*</sup> 

<sup>1</sup> Center on Nanoenergy Research, Institute of Science and Technology for Carbon Peak & Neutrality; Key Laboratory of Blue Energy and Systems Integration (Guangxi University), Education Department of Guangxi Zhuang Autonomous Region; School of Physical Science & Technology, Guangxi University, Nanning 530004, People's Republic of China

<sup>2</sup> Beijing Key Laboratory of Micro-Nano Energy and Sensor, Center for High-Entropy Energy and Systems, Beijing Institute of Nanoenergy and Nanosystems, Chinese Academy of Sciences, Beijing 101400, People's Republic of China

<sup>3</sup> School of Nanoscience and Technology, University of Chinese Academy of Sciences, Beijing 100049, People's Republic of China

E-mail: [yayang@binn.cas.cn](mailto:yayang@binn.cas.cn)

Received 6 February 2024, revised 11 March 2024

Accepted for publication 12 June 2024

Published 3 July 2024



## Abstract

At present, the research on ferroelectric photovoltaic materials mainly focuses on photoelectric detection. In the context of the rapid development of the Internet of Things (IoT), it is particularly important to use smaller thin-film devices as sensors. In this work, an indium tin oxide/bismuth ferrite (BFO)/lanthanum nickelate device has been fabricated on an F-doped tin oxide glass substrate using the sol-gel method. The sensor can continuously output photoelectric signals with little environmental impact. Compared to other types of sensors, this photoelectric sensor has an ultra-low response time of 1.25 ms and ultra-high sensitivity. Furthermore, a material recognition system based on a BFO sensor is developed. It can effectively identify eight kinds of materials that are difficult for human eyes to distinguish. This provides new ideas and methods for developing the IoT in material identification.

Supplementary material for this article is available [online](#)

Keywords: BiFeO<sub>3</sub>, ferroelectric materials, self-powered photodetector, material recognition

\* Author to whom any correspondence should be addressed.



Original content from this work may be used under the terms of the [Creative Commons Attribution 4.0 licence](#). Any further distribution of this work must maintain attribution to the author(s) and the title of the work, journal citation and DOI.

## 1. Introduction

With the rapid advancement of 5G and artificial intelligence (AI), the cost of transmitting data through wireless network technology has been greatly reduced. On this basis, the Internet of Things (IoT) has been developing rapidly [1]. Therefore, more and more sensors are deployed in various production and lifestyles, achieving great operational flexibility and convenience. This requires seamless interconnection between various physical components to ensure the uninterrupted data flow, and also ensure that flexible strategies are implemented to adapt to frequently changing adverse conditions. IoT is prevalent in various fields, such as healthcare, construction, agriculture, smart shopping, etc [2–10]. Sharma *et al* conducted in-depth research on the Internet of Vehicles by discussing the application of the Internet of Vehicles in different fields and conducted a comparative study on the Internet of Vehicles and vehicular ad-hoc network [11]. Wen *et al* proposed an AI-powered gesture recognition and speech communication system that includes sensing gloves, deep learning blocks, and virtual reality interfaces [12]. In healthcare, the proposed patient access control scheme by Luo *et al* involves a collaborative shared structure among multiple cloud servers to facilitate the provision of patient data to healthcare providers while ensuring the confidentiality of the data content [13]. In terms of smart shopping, Chojnacki and Rykowski proposed applying IoT devices and services and obtaining additional information about customer behavior and activity in real stores [14]. However, its use in these areas depends on the availability and use of various types of sensors. The speed and sensitivity of these sensors are also critical in their applications. Lee *et al* demonstrated a highly stretchable matrix of cross-reactive sensors that can detect, classify, and distinguish various mixed tactile and thermal stimuli using machine learning methods [15]. Mu *et al* proposed a biomimetic inductive finger (EM-Finger) that can be used in conjunction with triboelectric and visual sensing for remote control and tactile perception [10]. Qu *et al* developed a smart finger that goes beyond human tactile perception and can accurately identify material types [16].

Compared with the reported sensors for material identification, the photoelectric sensors have the advantages of short response time, high sensitivity, and high flexibility [17]. Wu *et al* reported a novel integrated logic gate that took advantage of the photoresponsiveness of multifunctional BiFeO<sub>3</sub> sensor materials. The bismuth ferrite (BFO) sensors are capable of not only detecting temperature and light intensity but also executing three basic logic gates by input light and heat to get an output electrical signal [18]. A temperature control and recording system were designed by Li *et al*. They used BaTiO<sub>3</sub> thin film to achieve direct measurement of pyroelectric output current [19]. The optoelectronic synapse constructed by Wang *et al* successfully simulates human visual perception and visual memory functions, providing new ideas for artificial neuro-morphic computing and artificial visual system in 2021 [20]. Yang *et al* built a neural network application that test recognition accuracy could reach 97.2% in 2024 [21].

In the investigated ferroelectric photovoltaic materials, BFO exhibits not only a high residual polarization but also

possesses a high Curie temperature. BFO has the characteristics of low crystallization temperature and narrow band gap [22]. Besides, it has many advantages such as environmental friendly (no emission of pollutants), no toxic materials (lead), self-powered, and many more. Therefore, BFO has received much attention in the field of ferroelectric photovoltaics. BFO is widely regarded as one of the most meaningful candidates for future use in emerging devices with multiple functions. The vigorous development of the microelectronics industry has led to a growing emphasis on miniaturization and integration, making thin film materials more suitable for the future advancement of this industry. In this work, a simple and inexpensive sol-gel method was used to construct the lanthanum nickelate (LNO, LaNiO<sub>3</sub>)/BFO/indium tin oxide (ITO) photoelectronic film structure on the F-doped tin oxide (FTO) glass substrate. The photoelectric sensor can maintain outstanding output signals in a wide range of light wavelengths, and the current is maximum in the ultraviolet band of 365 nm. The photoelectric sensor is greatly affected by light intensity, which also lays a foundation for the identification of transparent materials. The sensor can effectively identify eight transparent materials. The aforementioned statement holds significant implications for the future development of material identification utilizing inorganic ferroelectric thin films.

## 2. Results and discussion

In general, distinguishing different materials or objects is commonly based on visual perception through the naked eye most of the time in our daily life. This also has certain limitations, and it is difficult to distinguish between similar objects. It is led to the emergence of sensors. Figure 1(a) illustrates the innovation between this work and other approaches. Other work is often completed after the sensor comes into contact with the material to be measured. This work can be done in a contactless manner [10, 16]. The non-contact method can minimize the damage to the material and reduce the impact on the material. Other work can identify materials that are generally colored or have obvious differences in material that can be distinguished by the naked eye [16]. The materials to be tested in this work are all transparent colorless organic polymer materials, which are difficult to be distinguished by the naked eye. Other works mostly use triboelectric effect, thermoelectric effect, pyroelectric effect, and so on [23–26]. In this work, the photoelectric effect is used to identify materials. Photoelectric sensors can accurately distinguish materials. Because the speed of light travels extremely fast, the response time of photodetectors is shorter. The response time of most other sensors is greater than 40 ms [15, 24, 26–28], while the response time of the photodetector in this paper is only 1.25 ms, as shown in figure 1(b). Response time is an important index to measure sensor performance. With the development of science and technology, various types of sensors with shorter responses are forced to develop. For example, in autonomous driving, having a smaller response time can make it safer to deal with all kinds of emergencies. Such as, in automated factories, photoelectric sensors can be used for

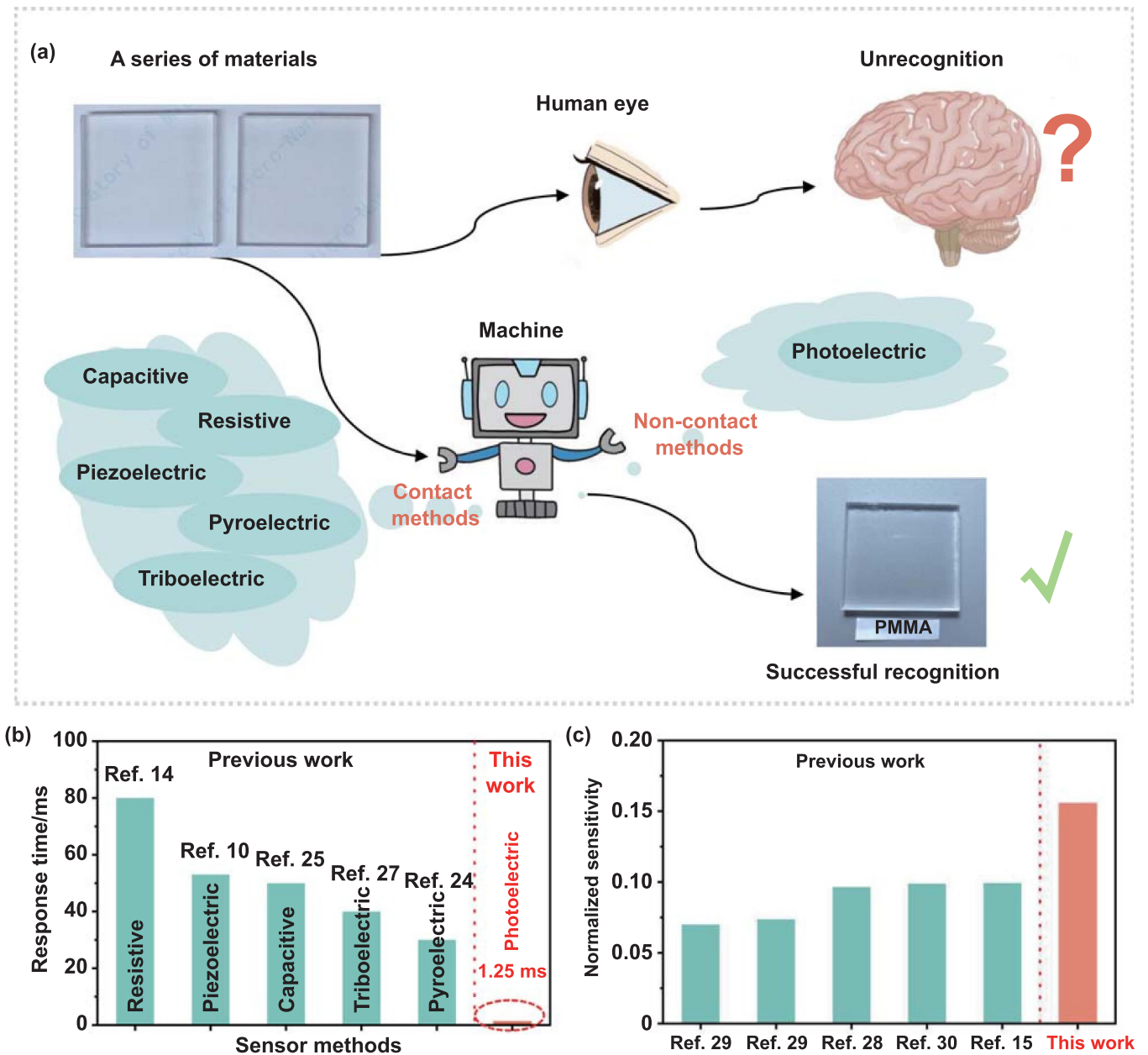


**Figure 1.** Innovation at work. (a) Innovation flow chart for this work. (b) Comparison of response time for this work with other works. (c) Sensitivity of this work to other work.

product quality inspection. Shorter response times can greatly improve productivity. Triboelectric and thermoelectric methods are most commonly used in research. But triboelectricity and thermoelectricity are susceptible to temperature and humidity in the environment. Therefore, they cannot have stable existence. The photoelectric sensor used in this study is not easily affected by the surrounding environment, and the light source is widely available. It provides the possibility for experimental conditions. Sensitivity also has a strong advantage over other conventional identification systems. After we normalized the sensitivity, the sensitivity of this work is much higher than that of other work [29–32], as shown in figure 1(c).

The calculation is in note S1. Light reaches the sensor after passing through the material to be measured, and different materials to be measured will produce different photoelectric signals. Through the analysis of the obtained photoelectric signal, the corresponding type of material to be measured can be obtained.

### 2.1. Device structure and characterization

The schematic of the BFO photoelectricity sensor is shown in figure 2(a), comprising a vertically stacked array of transparent ITO upper electrodes measuring  $2 \times 2$ , an

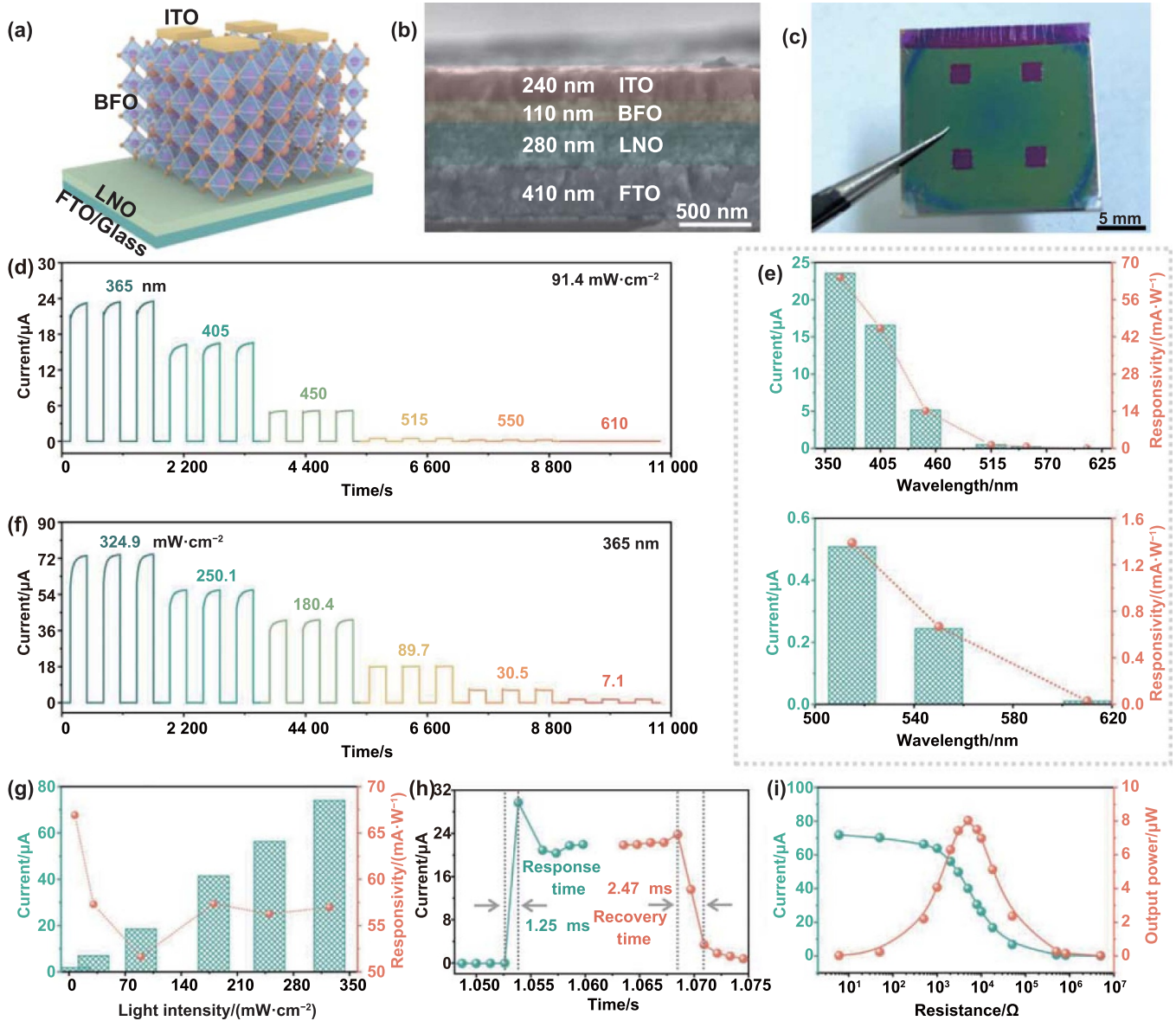


**Figure 2.** Structure and photoelectric signal of the ITO/BFO/LNO sensor. (a) Schematic diagram of BFO device. (b) SEM images of the microstructure of BFO device. (c) Photograph of the BFO device. (d) Photocurrent of the device under different light wavelengths with a light intensity of  $91.4 \text{ mW}\cdot\text{cm}^{-2}$ . (e) Photocurrents and corresponding responsivities as a function of wavelength. (f) Photocurrent of the device under different light intensities with a light wavelength of 365 nm. (g) Photocurrents and corresponding responsivities as a function of light intensity. (h) Response and recovery time under 365 nm light illumination. (i) Photocurrent and corresponding output power as a function of load resistance.

LNO lower electrode on an FTO glass substrate, and a BFO photoactive layer. The device possesses dimensions of  $20 \text{ mm} \times 20 \text{ mm} \times 1.6 \text{ mm}$ , with each ITO electrode exhibiting an area measuring  $2 \text{ mm} \times 2 \text{ mm}$ . The BFO film was prepared by a sol-gel process employing spin coating technology. Further details are provided in the method section. A physical diagram of the sensor is shown in figure 2(c). Figure 2(b) shows that the scanning electron microscopy (SEM) image of cross-sectional scan exhibits the exceptional uniformity and density of ITO, BFO, LNO, and FTO films with thicknesses

of 240 nm, 110 nm, 280 nm and 410 nm respectively. Figure S1 is the SEM image of the BFO surface, and it can be concluded that the grain size is uniform, and there are no apparent defects. The EDS spectra show that Bi, Fe, and O elements are uniformly distributed and the film quality is good. The direct band gap of BFO films is about 2.63 eV. It exhibits excellent sensitivity in the UV-visible range and has a wide range of absorption in the wavelength range of 350–500 nm. It can absorb many UV-visible photons (figure S2), providing a unique opportunity for photovoltaic applications.

## 2.2. Photoelectric properties of BFO films

Figure S4 is a schematic diagram of the test. The  $I$ – $V$  (current–voltage) characteristics of the BFO photosensor under both illuminated conditions ( $91.4 \text{ mW}\cdot\text{cm}^{-2}$ ) and dark conditions are presented in figure S5, with illuminating wavelengths ranging from 365 nm to 610 nm. The presence of nonlinear current–voltage ( $I$ – $V$ ) characteristics suggests the establishment of Schottky contacts between the electrodes and the BFO film. The BFO film, as a ferroelectric thin-film material with a low-band gap, has a significant response to light within the wavelengths range of 365 nm to 450 nm. It has a significant response. As shown in figures 2(d) and S7, a photocurrent of up to  $23.6 \mu\text{A}$  and a photovoltage of  $269 \text{ mV}$  ( $91.4 \text{ mW}\cdot\text{cm}^{-2}$ ) can be seen when the incident light is activated. It shows that the device has high light sensitivity. As the wavelength increases from 365 nm to 610 nm, the peak photocurrent and photovoltage decrease. It can be seen that the device has good absorption of short wavelengths. This is because short wavelength light has high energy and quantum efficiency. More photo-generated carriers transition from valence to conduction band. As shown in figure 2(e), the responsiveness decreases from approximately  $64.4 \text{ mA}\cdot\text{W}^{-1}$  to  $0.03 \text{ mA}\cdot\text{W}^{-1}$  as the optical wavelength increases from 365 nm to 610 nm. It can be seen that the device is more responsive at short wavelengths. Then, the different light intensities at 365 nm wavelength were investigated. As shown in figure 2(f), when the intensity of illumination decreases from  $324.9 \text{ mW}\cdot\text{cm}^{-2}$  to  $7.1 \text{ mW}\cdot\text{cm}^{-2}$ , the peak photocurrent decreases from  $74 \mu\text{A}$  to  $2 \mu\text{A}$ . The peak voltage is reduced from  $384 \text{ mV}$  to  $55 \text{ mV}$ , as shown in figure S8. As shown in figure 2(g), with the increase in light intensity, responsiveness showed a trend of decreasing and then increasing. The responsivity is maximum when the light intensity is  $7.1 \text{ mW}\cdot\text{cm}^{-2}$  and the value is  $67 \text{ mA}\cdot\text{W}^{-1}$ . When the intensity of illumination is  $89.7 \text{ mW}\cdot\text{cm}^{-2}$ , the value is  $51.7 \text{ mA}\cdot\text{W}^{-1}$ . The current responsivity  $R$  of the photodetector can be calculated according to the intensity of illumination and the corresponding photocurrent, and the calculation formula is

$$R = \frac{I_{\text{ph}} - I_{\text{d}}}{PS} \quad (1)$$

Here,  $I_{\text{ph}}$  represents the current under illumination,  $I_{\text{d}}$  is the dark current,  $P$  is the luminous flux density of incident light, and  $S$  is the effective area of the device [33].

The photodetector has a super-fast response time of 1.25 ms and a recovery time of 2.47 ms, as shown in figure 2(h). The ultra-short response time and recovery time are beneficial in preparing sensors, which can also lay the foundation for real-time detection. The output current was measured under various load resistances, decreasing with increasing resistance as illustrated in figure S9, to estimate the device's maximum output power. The output power was calculated according to the equation:

$$P = I^2 R \quad (2)$$

Here,  $P$  is the output power,  $I$  is the pyroelectric current and  $R$  is the load resistance [34]. Figure 2(i) shows that the output power was calculated. The maximum output power is  $8 \mu\text{W}$  at load resistances of  $5 \text{ K}\Omega$  respectively.

## 2.3. Output signals through different materials

To study the output signal of photoelectric sensors under different transparent materials. We used eight materials (PMMA, PS, Glass, PET, PVC, PETG, PU, ABS) (the thickness of the material is 10 mm) as test objects. When 365 nm UV light passes through the material to be tested (PMMA, PS, Glass, PET, PVC, PETG, PU, ABS) and irradiates onto the BFO sensor, the photoelectric current signals are  $70 \mu\text{A}$ ,  $60 \mu\text{A}$ ,  $58 \mu\text{A}$ ,  $26 \mu\text{A}$ ,  $19 \mu\text{A}$ ,  $16 \mu\text{A}$ ,  $1.6 \mu\text{A}$ , and  $0.9 \mu\text{A}$ , respectively. As shown in figure 3(a). The voltage signals are  $370 \text{ mV}$ ,  $357 \text{ mV}$ ,  $353 \text{ mV}$ ,  $270 \text{ mV}$ ,  $244 \text{ mV}$ ,  $220 \text{ mV}$ ,  $40 \text{ mV}$ , and  $30 \text{ mV}$ , respectively, as shown in figure 3(b). The transmittance of eight kinds of materials at wavelength 200–600 nm was tested, as shown in figure 3(c). At 365 nm light, the transmittances are 99.6%, 87.6%, 73.3%, 72.1%, 24.2%, 20.8%, 13.8%, 0.5%, and 0.02% (PMMA, PS, Glass, PET, PVC, PETG, PU, ABS), respectively. The same variation trend was found after comparing the transmittance and the photoelectric current, indicating that the photoelectric signal of the sensor is reliable, as shown in figure S6. These materials were tested under different lighting conditions, showing the same trend signal. It is sufficient to illustrate the stability and authenticity of the sensor output signal (as shown in figures S7–S17). Then, the sensitivity at transmittance is calculated and the value is  $0.77 \mu\text{A}/1\%$ . In figure 3(d), coefficient of determination ( $R^2 = 0.99226$ ) is very close to 1, indicating that the linear fitting effect is good. Then, the sensitivity of the photoelectric current relative to the 8 materials is calculated, and the value is  $10.8 \mu\text{A}/\text{Material}$ , as shown in figure 3(e). At this time, the coefficient of determination ( $R^2$ ) is 0.93927.

## 2.4. The working principle of the BFO photodetector

The working principle of the BFO device can be comprehended through an analysis of the energy band diagram depicted in figure 3(f). The volatilization of bismuth during heat treatment leads to the general classification of BFO thin film materials as P-type semiconductors. The ITO and LNO electrode materials have work functions of 4.8 eV and 4.5 eV [22, 35, 36], correspondingly (figure S3). The contact potential difference between the electrode and the BFO induces band bending at the interface, resulting in the formation of a contact barrier that significantly impacts the transfer of electron–hole pairs generated by photoexcitation. At 365 nm, BFO film absorbs photons, and valence electrons are pumped into the conduction band to create an electron–hole pair. The photoexcited electron–hole pair undergoes spatial separation due to the internal electric field induced by the barrier, resulting

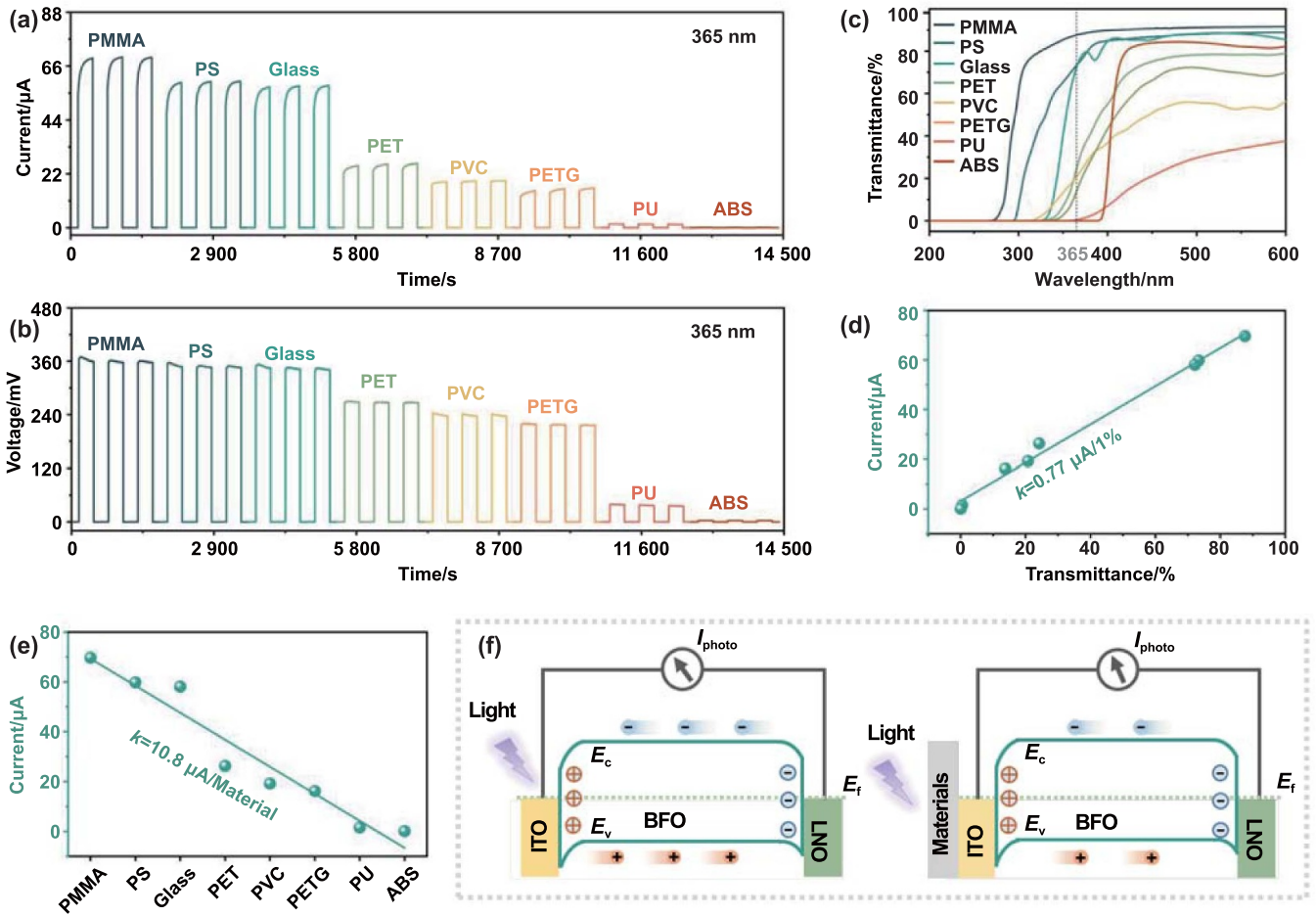


**Figure 3.** Output signals and working principles through different materials. (a) The photocurrent of 365 nm wavelength light passing through different materials. (b) The photovoltage of 365 nm wavelength light passing through different materials. (c) Transmittance of different materials. (d) Linear fit function of photocurrent with transmittance. (e) Linear fit function of photocurrent with material. (f) Mechanisms of device operation when light passes through materials.

in the formation of an individual electron and hole. It moved and accumulated to the ITO and LNO sides, correspondingly. Thus, a photocurrent can be generated in the external circuit from the LNO to the ITO.

The photoelectric signal is very different when the light passes through different materials. The different photoelectric signals are analyzed mechanically. When the light passes through different materials, the energy of the light reaching ITO is different, and some can produce more electron-hole pairs, which can move towards ITO and LNO sides, respectively. It shows a greater photocurrent externally. The other part is the opposite, as shown in figure 3(f).

**2.5. Construction of material identification system**

The optical image of 8 kinds of test materials is shown in figure 4(a). It can be observed that this material is

indistinguishable from the human eye. And our sensors are factories geared toward mass production. Therefore, the data of information is more conducive to production. Figure 4(b) is a photograph of the experimental setup. We control the light on and off to get the necessary photoelectric signal. We conducted 100 tests on 8 materials, and the test results are shown in figure S18. The results of each material are relatively stable, and there is no crossover phenomenon, which lays a good foundation for material identification. As shown in figure 4(c), the probability distribution statistics of 100 test results also show relatively good uniqueness. Then, the material identification system is designed, and the data from 8 kinds of materials are collected first. The maximum signal value of each material is extracted and sorted in order from largest to smallest (A1)–(A8). Then, the middle value between the maximum values is calculated, and between the two middle values is the numerical region of the material. When the test result is located in this area, it is the material [37], as shown in figure 4(d).

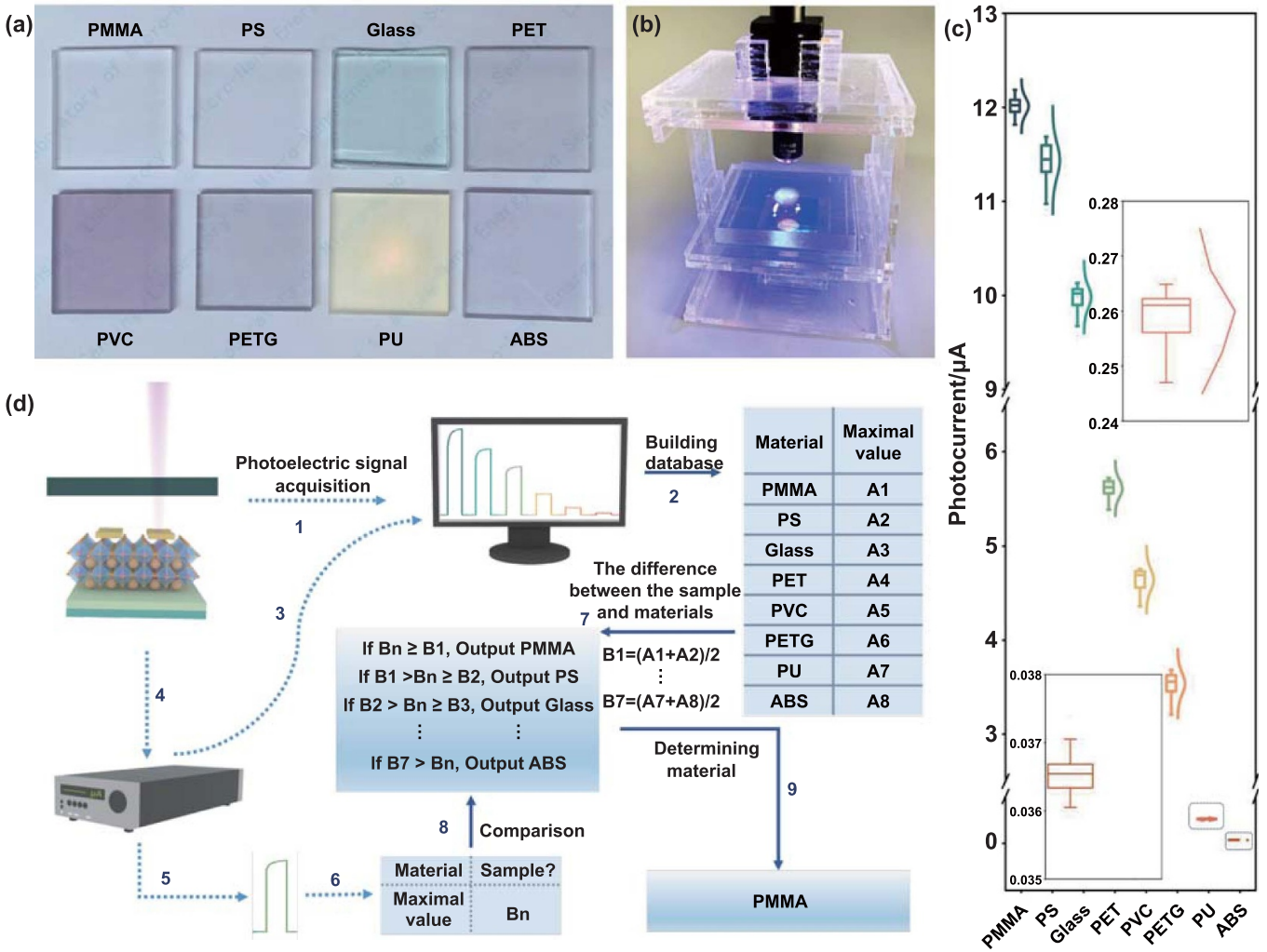


**Figure 4.** Material identification system. (a) Photographs of eight materials. (b) Photograph of the experimental setup. (c) Photocurrent through different materials. (d) The system consists of the training process (1–4) and the identification process (4–9).

### 3. Conclusions

In summary, the BFO thin film photodetector ITO/BFO/LNO was successfully constructed. The BFO thin film photodetector has an excellent light response of  $64.4 \text{ mA} \cdot \text{W}^{-1}$ . The BFO thin film photodetector has a very short response time of 1.25 ms and a recovery time of 2.47 ms. Compared to other types of sensors, photoelectric sensors have higher sensitivity. BFO photodetectors can identify transparent materials that are difficult for the human eye to distinguish. In material recognition applications, ferroelectric thin films have great potential in the future. This work offers a new way to investigate this research direction of the photodetector, which can further promote the development of research works on ferroelectric materials.

### 4. Methods

#### 4.1. Fabrication of precursor solutions

The precursor solution for synthesizing  $\text{BiFeO}_3$  (BFO) was obtained through the dissolution of 1.617 g of

$\text{Bi}(\text{NO}_3)_3 \cdot 5\text{H}_2\text{O}$  and 1.212 g of  $\text{FeN}_3\text{O}_9 \cdot 9\text{H}_2\text{O}$  in a mixture containing 0.5 ml of ethylene glycol and 15 ml of 2-methoxyethanol. The  $\text{BiFeO}_3$  precursor solution was successfully obtained by vigorously stirring at room temperature for 5 d, resulting in a stable and uniform solution.

The precursor solution for synthesizing  $\text{LaNiO}_3$  (LNO) was obtained through the dissolution of 1.4945 g  $\text{Ni}(\text{CH}_3\text{COO})_2 \cdot 4\text{H}_2\text{O}$  and 2.598 g  $\text{La}(\text{NO}_3)_3 \cdot 6\text{H}_2\text{O}$  in a mixture comprising 30 ml ethyl alcohol and 12 ml acetic acid at a temperature maintained at  $70^\circ\text{C}$ , with continuous stirring conducted over a period of 12 h.

#### 4.2. Fabrication of FTO glass/LNO/BFO/ITO device

A sol-gel process was used to create the LNO and BFO films, which were then fabricated using a spin coating technology. The deposition process of LNO film on FTO Glass substrate ( $13 \Omega\text{--}15 \Omega$ ,  $1.6 \text{ mm} \times 20 \text{ mm} \times 20 \text{ mm}$ ) involved spin-casting at 2000 rpm at room temperature, followed by sequential annealing at temperatures of  $180^\circ\text{C}$ ,  $400^\circ\text{C}$ , and  $700^\circ\text{C}$ . The deposition and annealing process was repeated

six times. The BFO film was spin-coated onto the LNO/FTO glass sample at a speed of 4000 rpm. The sample was then subjected to annealing at three different temperatures of 200 °C, 400 °C, and 550 °C respectively. The BFO film was coated and thermally annealed thrice. The 2 × 2 ITO (2 mm × 2 mm) electrode array was then deposited on the BFO/LNO/FTO glass sample using RF magnetron sputtering (150 W, 20 min).

#### 4.3. Characterizations and measurements

The microstructure was examined using SEM (Hitachi SU8020). A light-emitting diode was used to provide incident light. The photovoltage and photocurrent signals of the device were monitored via Keithley 2611B system Source Meter. The optical power density of the fabricated device is measured with a portable power meter (OPHIR, Starlite) as shown in figure S19. Absorption spectra and transmittance were tested using a UV–Vis–NIR spectrophotometer (UV3600).

#### Acknowledgments

This work was supported by the National Natural Science Foundation of China (Grant No. 52072041), the Beijing Natural Science Foundation (Grant No. JQ21007), and the University of Chinese Academy of Sciences (Grant No. Y8540XX2D2).

#### Conflict of interest

The authors declare no conflict of interest.

#### ORCID iD

Ya Yang  <https://orcid.org/0000-0003-0168-2974>

#### References

- [1] Wang J F, Suo J, Song Z X, Li W J and Wang Z B 2023 Nanomaterial-based flexible sensors for metaverse and virtual reality applications *Int. J. Extrem. Manuf.* **5** 032013
- [2] Hamza R, Yan Z, Muhammad K, Bellavista P and Titouna F 2020 A privacy-preserving cryptosystem for IoT E-healthcare *Inf. Sci.* **527** 493–510
- [3] Hassan A, Liu F, Wang F C and Wang Y 2021 Secure image classification with deep neural networks for IoT applications *J. Ambient Intell. Humaniz. Comput.* **12** 8319–37
- [4] Li C *et al* 2018 Analogue signal and image processing with large memristor crossbars *Nat. Electron.* **1** 52–59
- [5] Li K, Yuasa R, Utaki R, Sun M L, Tokumoto Y, Suzuki D and Kawano Y 2021 Robot-assisted, source-camera-coupled multi-view broadband imagers for ubiquitous sensing platform *Nat. Commun.* **12** 3009
- [6] Mekki K, Bajic E, Chaxel F and Meyer F 2019 A comparative study of LPWAN technologies for large-scale IoT deployment *ICT Express* **5** 1–7
- [7] Rajput S, Ippili A, Puraswani D, Johri S, Nadathur A and Dhar S 2020 Impact of earthquakes based on satellite images using IoT and sensor networks *Proc. 2020 Int. Conf. on Communication Systems & Networks* (IEEE)
- [8] Rathore M M, Son H, Ahmad A and Paul A 2018 Real-time video processing for traffic control in smart city using Hadoop ecosystem with GPUs *Soft Comput.* **22** 1533–44
- [9] Yao L N, Sheng Q Z, Benattallah B, Dustdar S, Wang X Z, Shemshadi A and Kanhere S S 2018 WITS: an IoT-endowed computational framework for activity recognition in personalized smart homes *Computing* **100** 369–85
- [10] Mu S L *et al* 2023 A platypus-inspired electro-mechanosensory finger for remote control and tactile sensing *Nano Energy* **116** 108790
- [11] Sharma S and Kaushik B 2019 A survey on internet of vehicles: applications, security issues & solutions *Veh. Commun.* **20** 100182
- [12] Wen F, Zhang Z X, He T Y Y and Lee C 2021 AI enabled sign language recognition and VR space bidirectional communication using triboelectric smart glove *Nat. Commun.* **12** 5378
- [13] Luo E T, Bhuiyan M Z A, Wang G J, Rahman A, Wu J and Atiqzaman M 2018 PrivacyProtector: privacy-protected patient data collection in IoT-based healthcare systems *IEEE Commun. Mag.* **56** 163–8
- [14] Chojnacki T and Rykowski J 2019 IoT-based surveillance for instant marketing in real stores *Information Systems Architecture and Technology: Proc. 39th Int. Conf. on Information Systems Architecture and Technology—ISAT 2018* ed L Borzemski, J Świątek and Z Wilimowska (Springer)
- [15] Lee J H *et al* 2020 A behavior-learned cross-reactive sensor matrix for intelligent skin perception *Adv. Mater.* **32** 2000969
- [16] Qu X C, Liu Z, Tan P C, Wang C, Liu Y, Feng H Q, Luo D, Li Z and Wang Z L 2022 Artificial tactile perception smart finger for material identification based on triboelectric sensing *Sci. Adv.* **8** eabq2521
- [17] Mao W Q, Li H N, Tang B, Zhang C, Liu L, Wang P, Dong H X and Zhang L 2023 Laser patterning of large-scale perovskite single-crystal-based arrays for single-mode laser displays *Int. J. Extrem. Manuf.* **5** 045001
- [18] Wu L, Ji Y, Dan H Y, Bowen C R and Yang Y 2023 A multifunctional optical-thermal logic gate sensor array based on ferroelectric BiFeO<sub>3</sub> thin films *InfoMat* **5** e12414
- [19] Li H Y, Bowen C R and Yang Y 2022 Phase transition enhanced pyroelectric nanogenerators for self-powered temperature sensors *Nano Energy* **102** 107657
- [20] Wang W X, Gao S, Li Y, Yue W J, Kan H, Zhang C W, Lou Z, Wang L L and Shen G Z 2021 Artificial optoelectronic synapses based on TiN<sub>x</sub>O<sub>2-x</sub>/MoS<sub>2</sub> heterojunction for neuromorphic computing and visual system *Adv. Funct. Mater.* **31** 2101201
- [21] Yang W H, Kan H, Shen G Z and Li Y 2024 A network intrusion detection system with broadband WO<sub>3-x</sub>/WO<sub>3-x</sub>-Ag/WO<sub>3-x</sub> optoelectronic memristor *Adv. Funct. Mater.* **34** 2312885
- [22] Yang L L, Wang X J, Bai L, Xu L and Yang Y 2023 Boosted photocurrent via heating BiFeO<sub>3</sub> thin film for UV photodetector at wide temperature range *Adv. Funct. Mater.* **33** 2303408
- [23] Xie M Y, Zhang Y, Kraśny M J, Bowen C, Khanbareh H and Gathercole N 2018 Flexible and active self-powered pressure, shear sensors based on freeze casting ceramic–polymer composites *Energy Environ. Sci.* **11** 2919–27
- [24] Yang T *et al* 2020 Hierarchically structured PVDF/ZnO core-shell nanofibers for self-powered physiological monitoring electronics *Nano Energy* **72** 104706
- [25] Park S *et al* 2014 Stretchable energy-harvesting tactile electronic skin capable of differentiating multiple mechanical stimuli modes *Adv. Mater.* **26** 7324–32

- [26] Li H Y, Bowen C R, Dan H Y and Yang Y 2024 Pyroelectricity induced by Schottky interface above the Curie temperature of bulk materials *Joule* **8** 401–15
- [27] Yoo J-Y, Seo M-H, Lee J-S, Choi K-W, Jo M-S and Yoon J-B 2018 Industrial grade, bending-insensitive, transparent nanoforce touch sensor via enhanced percolation effect in a hierarchical nanocomposite film *Adv. Funct. Mater.* **28** 1804721
- [28] Jiang X-Z, Sun Y-J, Fan Z Y and Zhang T-Y 2016 Integrated flexible, waterproof, transparent, and self-powered tactile sensing panel *ACS Nano* **10** 7696–704
- [29] Wang L Y, Liu Y M, Liu Q, Zhu Y Y, Wang H Y, Xie Z Q, Yu X G and Zi Y L 2020 A metal-electrode-free, fully integrated, soft triboelectric sensor array for self-powered tactile sensing *Microsyst. Nanoeng.* **6** 59
- [30] Huang J J, Wang S L, Zhao X K, Zhang W Q, Chen Z M, Liu R, Li P, Li H L and Gui C M 2023 Fabrication of a textile-based triboelectric nanogenerator toward high-efficiency energy harvesting and material recognition *Mater. Horiz.* **10** 3840–53
- [31] Zhao Z Y et al 2023 A broad range triboelectric stiffness sensor for variable inclusions recognition *Nano-Micro. Lett.* **15** 233
- [32] Zhao C, Wang Z Y, Wang Y W, Qian Z A, Tan Z, Chen Q Y, Pan X X, Xu M Y and Lai Y-C 2023 MXene-composite-enabled ultra-long-distance detection and highly sensitive self-powered noncontact triboelectric sensors and their applications in intelligent vehicle perception *Adv. Funct. Mater.* **33** 2306381
- [33] Ouyang B S, Zhao H Q, Wang Z L and Yang Y 2020 Dual-polarity response in self-powered ZnO NWs/Sb<sub>2</sub>Se<sub>3</sub> film heterojunction photodetector array for optical communication *Nano Energy* **68** 104312
- [34] Liu Y, Ji Y, Xia Y L, Wu L, Bowen C R and Yang Y 2022 Enhanced photocurrent in ferroelectric Bi<sub>0.5</sub>Na<sub>0.5</sub>TiO<sub>3</sub> materials via ferro-pyro-phototronic effect *Nano Energy* **98** 107312
- [35] Yang T-H, Harn Y-W, Chiu K-C, Fan C-L and Wu J-M 2012 Promising electron field emitters composed of conducting perovskite LaNiO<sub>3</sub> shells on ZnO nanorod arrays *J. Mater. Chem.* **22** 17071–8
- [36] Han X, Ji Y, Wu L, Xia Y L, Bowen C R and Yang Y 2022 Coupling enhancement of a flexible BiFeO<sub>3</sub> film-based nanogenerator for simultaneously scavenging light and vibration energies *Nano-Micro. Lett.* **14** 198
- [37] Wang Y, Wu H T, Xu L, Zhang H N, Yang Y and Wang Z L 2020 Hierarchically patterned self-powered sensors for multifunctional tactile sensing *Sci. Adv.* **6** eabb9083